

Stability of coalescing binary stars against gravitational collapse: hydrodynamical simulations

Masaru Shibata

Department of Earth and Space Science, Graduate School of Science, Osaka University, Toyonaka, Osaka 560-0043, Japan

Thomas W. Baumgarte

Department of Physics, University of Illinois at Urbana-Champaign, Urbana, IL 61801

Stuart L. Shapiro

Departments of Physics and Astronomy, and NCSA, University of Illinois at Urbana-Champaign, Urbana, IL 61801

We perform simulations of relativistic binary stars in post-Newtonian gravity to investigate their dynamical stability prior to merger against gravitational collapse in a tidal field. In general, our equations are only strictly accurate to first post-Newtonian order, but they recover full general relativity for spherical, static stars. We study both corotational and irrotational binary configurations of identical stars in circular orbits. We adopt a soft, adiabatic equation of state with $\Gamma = 1.4$, for which the onset of instability occurs at a sufficiently small value of the compaction M/R that a post-Newtonian approximation is quite accurate. For such a soft equation of state there is no innermost stable circular orbit, so that we can study arbitrarily close binaries. This choice still allows us to study all the qualitative features exhibited by any adiabatic equation of state regarding stability against gravitational collapse. We demonstrate that, independent of the internal stellar velocity profile, the tidal field from a binary companion stabilizes a star against gravitational collapse.

PACS number(s): 04.30.Db, 04.25.Nx, 97.60.Jd, 97.80.Fk

I. INTRODUCTION

Binary neutron stars are known to exist and for some of these systems in our own galaxy (including PSR B1913+16 and B1534+12), general relativistic effects in the binary orbit have been measured to high precision [1,2]. Interest in binary neutron stars has been stimulated by the prospect of future observations of extragalactic systems by gravitational wave interferometers like LIGO [3], VIRGO [4], TAMA [5] and GEO [6]. Binary neutron stars are among the most promising sources of gravitational waves for these detectors, and therefore it is important to predict theoretically the gravitational waveform emitted during the inspiral and the final coalescence of the two stars. Interest in these systems also arises on a more fundamental level, since the two-body problem is one of the outstanding unsolved problems in classical general relativity.

Considerable effort has gone into understanding binary neutron stars. Most of this work has been performed within the framework of Newtonian and post-Newtonian gravity (see, e.g., [7] for a review and list of references). General relativistic treatments are currently only in their infancy. Recently, Wilson, Mathews and Marronetti [8] (hereafter WMM) reported results obtained with a relativistic hydrodynamics code. Their code assumed several simplifying physical and mathematical approximations. Their results suggest that the central densities of the stars increase as the stars approach each other and that massive neutron stars, stable in isolation, individually collapse to black holes prior to merger. WMM therefore

find that in general relativity, the presence of a companion star and its tidal field tend to destabilize the stars in a binary system. This conclusion is contrary to what is expected from Newtonian [9], post-Newtonian [10–12], perturbative [13] and matched asymptotic expansion [14,15] treatments of the problem. Constructing self-consistent, fully relativistic initial data for two neutron stars in a circular, quasi-equilibrium orbit does not show any evidence of this “crushing effect” either [16]. Moreover, applying energy turning-point methods to sequences of these initial data suggests that inspiraling neutron star binaries are *secularly* stable all the way down to the innermost stable circular orbit [17]. To summarize, most researchers currently believe that the maximum allowed rest mass of neutron stars in close binaries is *larger* than in isolation, and that their central density is *smaller* than in isolation. If there exists any destabilizing, relativistic effect at high post-Newtonian order, then this effect is much smaller than the dominating stabilizing effect of the tidal field.

However, to date, the only fully *dynamical* treatment of the problem in general relativity – that of WMM – reports a star-crushing effect. In this paper, we perform a new, fully dynamical simulation for binary stars in post-Newtonian gravity. We use a formalism in which (1) all first post-Newtonian terms are taken into account, and (2) sufficient nonlinearity is retained, so that spherical, static stars satisfy the fully general relativistic equations exactly. As explained in section II below, this formalism is very suitable for studying binary neutron stars. We study relativistic effects in binary stars with $M/R \ll 1$,

where M and R are typical values of the stellar mass and radius, so that a post-Newtonian treatment is completely adequate.

By performing a fully dynamical calculation, we can relax various constraints assumed in previous treatments. For example, Wiseman assumed the stars to remain spherically symmetric [12], Baumgarte *et al.* [7] assumed the binary stars to be corotating, and Thorne [15] assumed the stars' orbital separation to be much larger than the stars' radius. Here, we relax all these assumptions and study tidally deformed stars, both corotational and irrotational, at arbitrarily small separations. We still find that the presence of the tidal field of a companion star tends to stabilize neutron stars against catastrophic collapse.

To establish the stability of binary stars against collapse, we construct quasi-equilibrium initial data for identical binary neutron stars in a close, circular orbit. The idea is to show whether stars in a binary formed from the inspiral of objects which are stable in isolation remain stable at close separation. Our models have rest masses near the maximum allowed rest mass for spherical stars in isolation and thus provide the best candidates for collapse if the tidal field is destabilizing (stars with rest masses well below the maximum allowed value are unambiguously stable). In order to demonstrate that these stars are dynamically stable, we need to locate the onset of instability in the binary, and compare it with the onset of instability for isolated stars. Since the shift is fairly small, a very careful treatment with high numerical accuracy is necessary. We detail our method of locating the onset of instability in section IV.

The paper is organized as follows: In section II, we present the post-Newtonian formalism adopted in this paper. We calibrate our code in section III by locating the analytically known onset of radial instability of relativistic spherical stars against gravitational collapse [18]. In section IV, we study the dynamical stability against gravitational collapse of close binary stars, and briefly summarize our results in section V.

II. FORMULATION

In the usual post-Newtonian treatment, the fluid and field equations are derived by systematically expanding the Einstein equation and the relativistic hydrodynamic equations in powers of c^{-1} [19]. In this paper, we introduce a different approach. Since in a first order post-Newtonian approximation, the spatial metric γ_{ij} may always be chosen conformally flat, we can derive post-Newtonian equations by starting with the relativistic equations written previously in the conformally flat approximation [8,7]. We then neglect some of the second and higher order post-Newtonian terms, but retain sufficient nonlinearity so that this formalism recovers full general relativity for some limiting regimes of interest in

this paper.

We write the spatial metric in the form

$$\gamma_{ij} = \psi^4 \tilde{\gamma}_{ij} = \psi^4 \delta_{ij}, \quad (2.1)$$

so that the line element becomes

$$ds^2 = g_{\mu\nu} dx^\mu dx^\nu = (-\alpha^2 + \beta_k \beta^k) dt^2 + 2\beta_i dx^i dt + \psi^4 \delta_{ij} dx^i dx^j. \quad (2.2)$$

Here, α , β_i and ψ are the lapse function, the shift vector and the conformal factor and we adopt geometrized units in which $c \equiv 1 \equiv G$. We also adopt cartesian coordinates $x^i = (x, y, z)$, so that the covariant derivative $\tilde{\nabla}_k$ associated with $\tilde{\gamma}_{ij} = \delta_{ij}$ conveniently reduces to the ordinary partial derivative $\partial/\partial x^k$.

We employ a perfect fluid stress-energy tensor

$$T^{\mu\nu} = \rho \left(1 + \varepsilon + \frac{P}{\rho} \right) u^\mu u^\nu + P g^{\mu\nu}, \quad (2.3)$$

where ρ , ε , P , and u^μ denote the rest mass density, specific internal energy, pressure, and the fluid four velocity, respectively. For initial data, we assume a constant entropy configuration with a polytropic pressure law

$$P = K \rho^\Gamma, \quad (2.4)$$

where K and $\Gamma = 1 + 1/n$ are constant and n is the polytropic index. For the evolution of the matter we assume the adiabatic relation

$$P = (\Gamma - 1) \rho \varepsilon. \quad (2.5)$$

The continuity equation is

$$\frac{\partial \rho_*}{\partial t} + \frac{\partial(\rho_* v^i)}{\partial x^i} = 0, \quad (2.6)$$

where $\rho_* = \rho \alpha u^0 \psi^6$ and $v^i = u^i/u^0$.

The relativistic Euler equation is

$$\begin{aligned} \frac{\partial(\rho_* \tilde{u}_i)}{\partial t} + \frac{\partial(\rho_* \tilde{u}_i v^j)}{\partial x^j} = & -\alpha \psi^6 P_{,i} - \rho_* \alpha \tilde{u}^0 \alpha_{,i} \\ & + \rho_* \tilde{u}_j \beta^j_{,i} + \frac{2\rho_* \tilde{u}_k \tilde{u}_k}{\psi^5 \tilde{u}^0} \psi_{,i}, \end{aligned} \quad (2.7)$$

and the energy equation is

$$\frac{\partial e_*}{\partial t} + \frac{\partial(e_* v^j)}{\partial x^j} = 0, \quad (2.8)$$

where

$$\tilde{u}_j = (1 + \Gamma \varepsilon) u_j, \quad (2.9)$$

$$\tilde{u}^0 = (1 + \Gamma \varepsilon) u^0, \quad (2.10)$$

$$e_* = (\rho_* \varepsilon_*)^{1/\Gamma}; \varepsilon_* = \varepsilon (\alpha u^0 \psi^6)^{\Gamma-1}, \quad (2.11)$$

$$v^i = -\beta^i + \frac{u_j}{\psi^4 u^0}. \quad (2.12)$$

Note that $\beta^i = \psi^{-4}\beta_i$ in the conformal flat approximation. From the normalization condition $u^i u_i = -1$, we find

$$\begin{aligned} (\alpha u^0)^2 &= 1 + \frac{u_i u_i}{\psi^4} \\ &= 1 + \frac{\tilde{u}_i \tilde{u}_i}{\psi^4} \left[1 + \Gamma \frac{\varepsilon_*}{(\alpha u^0 \psi^6)^{\Gamma-1}} \right]^{-2}. \end{aligned} \quad (2.13)$$

In our numerical simulation, we use ρ_* , \tilde{u}_i , and e_* as the independent variables that are determined by the hydrodynamical equations.

Equations for ψ , β^i and α can be found from the Hamiltonian constraint, the momentum constraint, and the maximal slicing condition $\text{tr}K = 0$, where $\text{tr}K$ is the trace of the extrinsic curvature K_{ij} (details can be found, for example, in [7]).

Assuming maximal slicing for all times, we have $\partial_t \text{tr}K = 0$, and can use the trace of the evolution equation for K_{ij} to find

$$\Delta(\alpha\psi) = 2\pi\alpha\psi^5 \left(E + 2S_{ij}\delta^{ij}\psi^{-4} \right) + \frac{7}{8}\alpha\psi^5 K_{ij}K^{ij}. \quad (2.14)$$

Here $E = \rho(1 + \Gamma\varepsilon)(\alpha u^0)^2 - P$, $S_{ij} = T_{ij}$, and Δ is the flat space Laplacian.

Since we assume the spatial metric to remain conformally flat for all times, the trace free part of the time evolution equation for γ_{ij} has to vanish, which yields

$$2\alpha\psi^{-4}K_{ij} = \delta_{il}\beta^l_{,j} + \delta_{jl}\beta^l_{,i} - \frac{2}{3}\delta_{ij}\beta^l_{,l}. \quad (2.15)$$

This equation shows that the extrinsic curvature no longer represents independent dynamical degrees of freedom (i.e., it may no longer exactly satisfy its fully relativistic evolution equation). Inserting this into the momentum constraint, $(\psi^6 K^i_{,j})_{,i} = 8\pi J_j \psi^6$, where $J_i = \rho_* \tilde{u}_i \psi^{-6}$, we find

$$\begin{aligned} \Delta\beta^i + \frac{1}{3}\beta^j_{,ji} &= \left[\ln\left(\frac{\alpha}{\psi^6}\right) \right]_{,j} \left(\beta^i_{,j} + \beta^j_{,i} - \frac{2}{3}\delta_{ij}\beta^l_{,l} \right) \\ &+ 16\pi\alpha J_i. \end{aligned} \quad (2.16)$$

Finally, the Hamiltonian constraint yields

$$\Delta\psi = -2\pi\psi^5 E - \frac{K_{ij}K^{ij}\psi^5}{8}. \quad (2.17)$$

For the post-Newtonian point of view assumed here, a conformally flat spatial metric takes into account all Newtonian and first post-Newtonian terms, and differences from a general, fully nonlinear metric appear at second post-Newtonian order [20,21]. We can therefore use the above equations, which assume a conformally flat metric, as a starting point for a post-Newtonian approximation. We simplify the problem by neglecting other terms of second or higher post-Newtonian order. In particular, we will neglect the nonlinear terms

$7\alpha\psi^5 K_{ij}K^{ij}/8$, $[\ln(\alpha\psi^{-6})]_{,j}(\beta^i_{,j} + \beta^j_{,i} - 2\delta_{ij}\beta^l_{,l}/3)$, and $K_{ij}K^{ij}\psi^5/8$. Note that for static, spherically symmetric spacetimes, these terms vanish identically, so that we still recover full general relativity for these spacetimes.

Adopting this approximation, the field equations reduce to

$$\Delta(\alpha\psi) = 2\pi\alpha\psi^5 \left(E + 2S_{ij}\delta^{ij}\psi^{-4} \right) \equiv 4\pi S_{\alpha\psi}, \quad (2.18)$$

$$\Delta\beta^i + \frac{1}{3}\beta^j_{,ji} = 16\pi\alpha J_i, \quad (2.19)$$

$$\Delta\psi = -2\pi\psi^5 E \equiv 4\pi S_\psi. \quad (2.20)$$

We decompose the equation for β^i using

$$\beta^i = 4B_i - \frac{1}{2} \left[\chi_{,i} + (B_k x^k)_{,i} \right] \quad (2.21)$$

so that B_i and χ satisfy

$$\Delta B_i = 4\pi\alpha J_i, \quad (2.22)$$

$$\Delta\chi = -4\pi\alpha J_i x^i. \quad (2.23)$$

To summarize, we have reduced Einstein's equations to six elliptic equations for the six functions $\alpha\psi$, ψ , B_i and χ . We solve these equations together with the boundary conditions

$$\alpha\psi = 1 - \frac{1}{r} \int S_{\alpha\psi} dV + O(r^{-3}), \quad (2.24)$$

$$\psi = 1 - \frac{1}{r} \int S_\psi dV + O(r^{-3}), \quad (2.25)$$

$$\begin{aligned} B_x &= -\frac{x}{r^3} \int \alpha J_x x dV - \frac{y}{r^3} \int \alpha J_x y dV \\ &+ O(r^{-4}), \end{aligned} \quad (2.26)$$

$$\begin{aligned} B_y &= -\frac{x}{r^3} \int \alpha J_y x dV - \frac{y}{r^3} \int \alpha J_y y dV \\ &+ O(r^{-4}), \end{aligned} \quad (2.27)$$

$$B_z = -\frac{z}{r^3} \int \alpha J_z z dV + O(r^{-4}), \quad (2.28)$$

$$\chi = \frac{1}{r} \int \alpha J_i x^i dV + O(r^{-3}), \quad (2.29)$$

where dV is the coordinate volume element. Note that having removed some of the nonlinear terms from the elliptic equations (2.18) to (2.23), their right hand sides now have compact support. This further simplifies the computations, since in imposing the boundary conditions at a finite separation, we do not truncate any source terms in (2.18) to (2.23) that extend to infinity.

Having neglected some second post-Newtonian terms, our formalism is strictly only first-order post-Newtonian. Note, however, that we have only truncated some of the non-linear terms in the field equations, pieces of which, loosely speaking, can be associated with dynamical features of the gravitational fields. In particular, we still solve the fully relativistic hydrodynamic equations. We

therefore retain many of the nonlinear features of full general relativity, and expect that this formalism provides an excellent approximation in several limiting regimes of interest here.

For example, for static, spherically symmetric stars, we recover the fully relativistic, Oppenheimer-Volkov solution. This is, because we can choose coordinates such that all the terms neglected in the field equations vanish identically, and the equations of hydrodynamics (or, in this case, hydrostatics) are fully relativistic. Constructing sequences of equilibrium solutions, we can apply the energy turning point method and find the onset of radial instability – again without approximation.

Corotational or irrotational binary stars at large separations are very close to being spherically symmetric because the two stars interact only through weak tidal fields (for example, in Newtonian case, see refs. [9,22]). Hence, our formalism can describe the individual stars to high accuracy, whether or not the stars are very compact and have strong gravitational fields. We therefore expect that our approximations are quite adequate.

In a binary in which the orbital separation a is large compared to the stellar radius R , we can treat the gravitational effects and tidal deformation due to the companion star as a small perturbation. We can then expand the gravitational field around the unperturbed, spherical solution [14,15]

$$\alpha = {}_{(0)}\alpha + {}_{(2)}\alpha\epsilon^2 + {}_{(4)}\alpha\epsilon^4 + {}_{(5)}\alpha\epsilon^5 + {}_{(6)}\alpha\epsilon^6 + {}_{(7)}\alpha\epsilon^7 + \dots, \quad (2.30)$$

$$\psi = {}_{(0)}\psi + {}_{(2)}\psi\epsilon^2 + {}_{(4)}\psi\epsilon^4 + {}_{(5)}\psi\epsilon^5 + {}_{(6)}\psi\epsilon^6 + {}_{(7)}\psi\epsilon^7 + \dots, \quad (2.31)$$

$$\beta^i = {}_{(1)}\beta^i\epsilon + {}_{(3)}\beta^i\epsilon^3 + {}_{(5)}\beta^i\epsilon^5 + {}_{(6)}\beta^i\epsilon^6 + {}_{(7)}\beta^i\epsilon^7 + {}_{(8)}\beta^i\epsilon^8 + \dots, \quad (2.32)$$

$$\tilde{\gamma}_{ij} = \delta_{ij} + {}_{(2)}h_{ij}\epsilon^2 + {}_{(4)}h_{ij}\epsilon^4 + {}_{(5)}h_{ij}\epsilon^5 + \dots, \quad (2.33)$$

where we assume

$$v^i \sim u_i \sim (M/a)^{1/2} \lesssim (R/a)^{1/2} \sim \epsilon, \quad (2.34)$$

and where M is gravitational mass, and ${}_{(0)}\alpha$ and ${}_{(0)}\psi$ denote the spherical symmetric solutions [23]. Note that ϵ denotes the magnitude of gravitational effects from the companion star, and hence the expansion in terms of ϵ is different from a post-Newtonian expansion (see [14].)

In our formalism, we can calculate ${}_{(0)}\alpha$ and ${}_{(0)}\psi$ exactly. Newtonian and first post-Newtonian terms appearing in ${}_{(n)}\alpha$, ${}_{(n)}\psi$ and ${}_{(n)}\beta^i$ for $n \neq 0$ are also taken into account consistently for all order in ϵ , although second post-Newtonian terms in these and ${}_{(n)}h_{ij}$ are not included. Our approximation is therefore appropriate for investigating the stability of fully general relativistic spherical stars due to Newtonian and first post-Newtonian tidal effects, which is our goal in this paper.

Details of our numerical methods, for solving both the hydrodynamical equations and the Poisson equations,

can be found in [24]. We assume symmetry with respect to equatorial plane, and solve the equations on a uniform grid of size $(2N + 1, 2N + 1, N + 1)$, covering the physical space $-L \leq x, y \leq L$ and $0 \leq z \leq L$ where L is location of outer boundaries. We use $N = 50$ for the spherical symmetric stars, and $N = 50, 60,$ and 75 for binary configurations.

As a numerical check, we monitor the conservation of proper mass

$$M_p = \int \rho_* dV, \quad (2.35)$$

total gravitational mass

$$M \equiv -2 \int S_\psi dV, \quad (2.36)$$

and total angular momentum

$$J \equiv \int (-yJ_x + xJ_y)\psi^6 dV. \quad (2.37)$$

Our difference scheme guarantees conservation of M_p exactly. Accurate conservation of M and J depends on N , and for $N = 75$, the error in one orbital period is $\lesssim 0.05\%$ for M and $\lesssim 0.5\%$ for J , respectively.

III. DYNAMICAL STABILITY OF SPHERICAL STATIC STARS

In this section we calibrate our code by locating the analytically known onset of instability of spherical equilibrium stars.

For initial conditions, we construct sequences of equilibria satisfying the Oppenheimer-Volkov equations. Note that for these configurations our formalism is exact and recovers the fully relativistic solutions. In Fig. 1 we show the proper mass M_p and the (isotropic) coordinate radius R as a function of the central density ρ_c for a polytrope with $\Gamma = 1.4$ ($n = 2.5$). We have taken advantage of the scale freedom in the problem and chosen $K = 1$. Together with $c = 1 = G$, this assignment uniquely determines our non-dimensional units for length, mass, etc.. For any other value of K , all the results can be rescaled trivially (see, e.g., [16]). Note that for a critical central density $\rho_c = \rho_{\text{crit}} (\simeq 1.2 \times 10^{-4})$, the mass M_p goes through a maximum $M_{\text{max}} \sim 1.248$. This maximum marks the onset of radial instability, and separates the stable branch ($\rho_c < \rho_{\text{crit}}$) from the unstable branch ($\rho_c > \rho_{\text{crit}}$) of the sequence.

For $\Gamma = 1.4$, the compaction of the maximum mass configuration, $M_p/R|_{\text{crit}} \sim 0.03$, is much less than unity (recall $M_p/R|_{\text{crit}} \rightarrow 0$ as $\Gamma \rightarrow 4/3$). Nevertheless, the mass versus central density equilibrium curve still exhibits an extremum, and therefore has all the qualitative features of any value of $\Gamma > 4/3$ regarding the issue of radial stability. Choosing $\Gamma = 1.4$ therefore allows us to

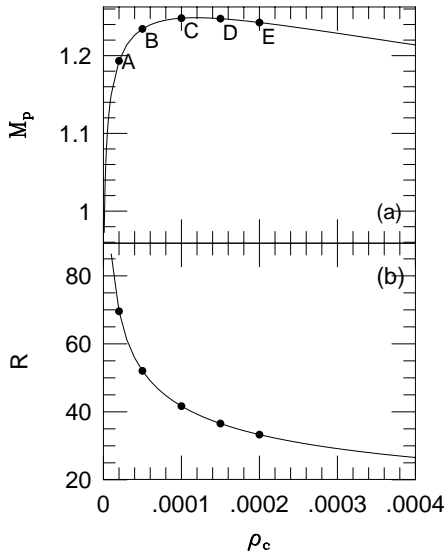


FIG. 1. Proper mass M_p (top panel) and isotropic radius R (bottom panel) as a function of central density ρ_c for relativistic, spherical polytropes with $\Gamma = 1.4$.

study these qualitative features in a regime in which the post-Newtonian approximation is very reliable.

Consider results for five different initial configurations, which we denote by A, B, C, D and E (see Fig. 1). We construct these initial data with a one-dimensional integration of the Oppenheimer-Volkov equations. These data are in equilibrium according to the one-dimensional finite difference equations. Interpolating these data onto the three-dimensional grid of our evolution scheme introduces a slight perturbation of the equilibrium solution, since the truncation error of the three-dimensional finite difference equations is different from the one-dimensional one. Typically, we find that the pressure of the interpolated models is slightly larger than the required equilibrium value on the three-dimensional grid. We compensate for that by artificially decreasing the polytropic constant K by a small amount. Note that our finite differencing is convergent, so that for finer grids we need to change K by smaller amounts. For the results presented here, the initial radius of the star is covered by 30 grid points.

Note that because of the scale freedom in the problem, reducing K is equivalent to increasing the mass. This is, because $K^{n/2}$, where n is the polytropic index, has units of mass (or length) in geometrized units. Consider now a model in which we have reduced K by, say, a small fraction $\delta \ll 1$. We can then rescale this model in order to investigate a different K , for example, the original value $K = 1$. Then, the mass of the re-scaled model has to increase by a fraction $n\delta/2$ to remain in equilibrium. For example, reducing K by 0.5 % is, for $n = 2.5$, equivalent

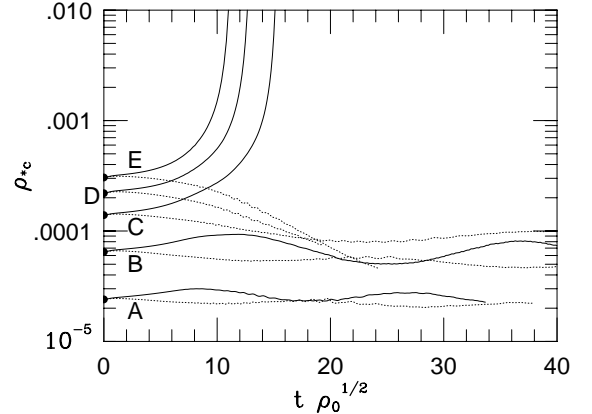


FIG. 2. Time evolution of ρ_* at center of stars for models A – E.

to increasing the model’s mass by 0.625 %.

We can now test the stability of our models by varying K by small amounts. Small variations in K serve to trigger small initial perturbations away from equilibrium (e.g. “pressure depletion”). Stable models will not change their qualitative behavior, whereas unstable models will. In Fig. 2 we show the time evolution of the central density ρ_* for the five models. Solid curves are the results for $K = 0.995$, and dotted curves are for $K = 1$. In this section, we plot time in units of $\rho_0^{-1/2}$, where ρ_0 is the central value of ρ of the corresponding spherical equilibrium star.

Obviously, models A and B oscillate stably, for both values of K . The period of these oscillations can be compared with the approximate analytic value [25]

$$t_{\text{osc}} \simeq 2\pi \left[\frac{3(\Gamma - 1)M^2}{(5\Gamma - 6)RI} \left(3\Gamma - 4 - 6.75 \frac{M}{R} \right) \right]^{-1/2}, \quad (3.1)$$

where M is the Newtonian (rest) mass, R is the Newtonian radius of star, and

$$I = \int \rho r^2 dV \quad (3.2)$$

is the spherical mass moment. Inserting the values $\rho_c \simeq 5.6M/R^3$ and $I \simeq 0.17MR^2$ for $\Gamma = 1.4$, we find

$$t_{\text{osc}} \simeq 5.5\rho_c^{-1/2} \left(0.2 - 6.75 \frac{M}{R} \right)^{-1/2}. \quad (3.3)$$

For model A, $M/R \simeq 0.017$ and hence $t_{\text{osc}} \simeq 18\rho_c^{-1/2}$, which is very close to the value that can be read off in

Fig. 2. Obviously, models with a larger compaction M/R have, in units of $\rho_c^{-1/2}$, a larger oscillation period t_{osc} , which can also be seen in Fig. 2. At the onset of instability, $t_{\text{osc}} \rightarrow \infty$. From equation (3.3) we therefore find that the maximum mass configuration must have a compaction $M/R \simeq 0.029$, which is very close to that of model C.

Leaving $K = 1$ for model C, the star oscillates stably, but reducing K by only 0.5 % to 0.995, the central density increases monotonically, and the star undergoes gravitational collapse. This indicates that model C is marginally stable against small perturbations, $\delta K/K \lesssim 0.5\%$, and very close to the onset of instability. This is obviously true, since its proper mass is only 0.05% smaller than the maximum allowed mass M_{max} .

For models D and E, the star monotonically expands or collapses, and never oscillates: starting with $K = 0.995$, the star collapses, and for $K = 1$, the star expands by a large factor [26]. Obviously, for $K = 1$ the star should be in equilibrium, and neither expand nor collapse. The equilibrium is unstable, however, and even the smallest truncation error induces a growing perturbation, which must ultimately lead to gravitational collapse. Initially, this perturbation may be either an expansion or a contraction. Since the configuration is gravitationally bound, the expansion soon has to turn around and lead to gravitational collapse [26]. Obviously, we would expect that for $K > 1$ we find an initial expansion, and for $K < 1$ an immediate contraction. However, due to truncation error, the cutoff between expansion and contraction is not precisely at $K = 1$, but instead at a value slightly smaller than unity ($K \simeq 0.997$ when we use 30 grid points to cover the star). Again, this value approaches unity with increasing grid resolution. This behavior establishes that models D and E are unstable to radial perturbations, which is, of course, what we expected.

We conclude that we can locate the onset of radial instability, and in particular that we can determine the maximum allowed mass of neutron stars to very high accuracy. This will be very important for determining the stability properties of binary neutron stars.

IV. DYNAMICAL STABILITY OF STARS IN BINARY SYSTEMS

In this section we present numerical results on the dynamical stability of stars in binary systems. We always assume the two stars to have equal mass, and set up initial data so that they are in a circular binary orbit. Note that for $\Gamma = 1.4$ the equation of state is sufficiently soft, so that there is no innermost stable circular orbit [9,27,7]. Therefore, we can choose arbitrarily small binary separations, and the *orbit* of the binary will still be stable. We choose very close binaries, in which the separation of the surfaces of the two stars is much smaller than the

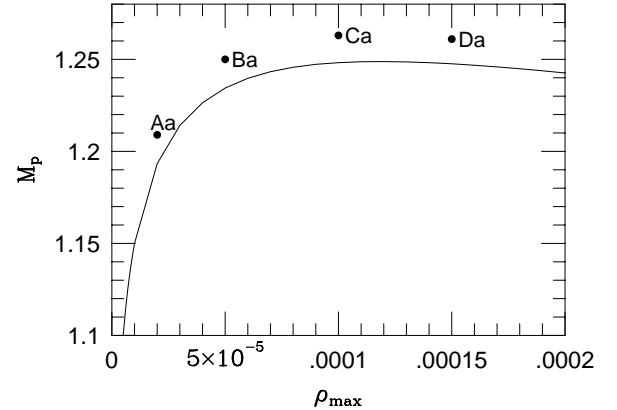


FIG. 3. Proper mass as a function of the maximum density for each star in a corotational equilibrium binary (filled circles) and for an isolated spherical star (solid line).

orbital separation ($z_A \simeq 0$ in the terminology of ref. [7]). For these binaries the tidal effects are strongest, and they are therefore the most suitable configuration to study the stability against gravitational collapse of the individual stars.

We evolve three different classes of binary initial data. The first class are corotational binaries. For these configurations, self-consistent equilibrium initial data can be constructed in post-Newtonian approximation [27] and even in general relativity (where the stars are only in quasi-equilibrium, see [16,7]). We denote the class of post-Newtonian strict equilibrium solutions with a subscript “a”.

In addition to corotational binaries, we would also like to study irrotational binaries because they are more realistic models for binary neutron stars [28]. Self-consistent irrotational equilibrium binaries in Newtonian gravity have recently been constructed by Uryu and Eriguchi [29], and a relativistic generalization has been suggested by Bonazzola, Gourgoulhon and Marck [30]. No numerical models are currently available for such data in a post-Newtonian approximation. In the absence of self-consistent, tidally deformed equilibrium data, we therefore take two spherically symmetric stars, put them close together, and artificially assign an irrotational velocity profile which maintains their shape and circular orbit approximately. In order to *calibrate* these irrotational initial data, which are not strictly in equilibrium, we first perform simulations with a second class of corotational initial data, using spherically symmetric stars, and compare these with the self-consistent post-Newtonian

equilibrium models which exist in the corotational case. For this second class, we assign a uniform velocity

$$(u_x, u_y, u_z) = (-\Omega y, \Omega x, 0) \quad (4.1)$$

to each fluid particle, where Ω is the orbital angular velocity. We denote these corotational, near-equilibrium data with a subscript “b”.

Finally, the third class of initial data are irrotational, near-equilibrium models. Again, we put two spherically symmetric stars at a small separation, but now we assign an initial velocity

$$(u_x, u_y, u_z) = \left(0, \pm\Omega x_0, 0\right) \quad (4.2)$$

to each fluid particle [31]. The centers of mass of the two stars are located at $(\pm x_0, 0, 0)$, where $x_0 > 0$. The plus sign in (4.2) corresponds to the star at $(+x_0, 0, 0)$, and vice versa. We denote this third class of initial data with a subscript “c”.

In the above velocity profiles, we determine the angular velocity Ω from Kepler’s law

$$\Omega = \left(\frac{M_T}{a^3}\right)^{1/2} \quad (4.3)$$

where $M_T = 2M_p$ is the sum of the proper mass of the two spherical stars and a is the coordinate separation between their centers of mass.

In the above velocity profiles, it would be more physical to fix v^i instead of u_i . That, however, would involve one more iteration in the preparation of the initial data, and, in our small compaction cases, would make only a negligible difference. We summarize the initial conditions for six different models, two in each class, in Table I.

As in our spherical models, we must vary K slightly in order to investigate the stability of the binary models. Equilibrium stars in tidal fields are tidally deformed and have a slightly smaller central density than spherical stars. Using spherical models as initial data for binaries therefore overestimates the central density, which causes the stars to expand initially. As we will see, this can be compensated for by reducing K .

A. Corotational equilibrium models

Following Shibata [27] and Baumgarte *et al.* [7,16], we construct self-consistent equilibrium initial data, describing two corotational binary stars in contact ($z_A = 0$). In Fig. 3, we plot the proper mass of each star as a function of the central density (filled circles), and compare these values with those for spherical stars in isolation (solid line). The maximum allowed mass of binary stars is slightly *larger* than that of spherical stars in isolation (see the discussion in [7]).

We show results for grid sizes $N = 40, 50, 60$, and 75, and find that our code is second order accurate. The

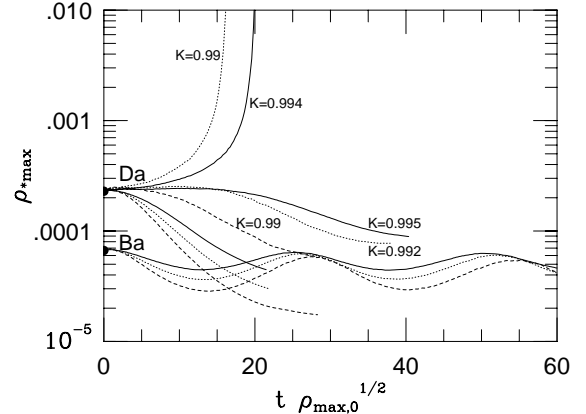


FIG. 4. Time evolution of ρ_{*max} in the corotational equilibrium binary models Ba and Da. Solid, dotted and dashed lines denote results obtained with $N = 75, 60$, and 50 grid-points, respectively. For model Ba, we set $K = 1$ initially. For model Da, initial values of K are 1, 0.995 and 0.994 for $N = 75$; 1, 0.992 and 0.99 for $N = 60$; and 1 and 0.99 for $N = 50$. Curves with numerical labels show values of $K \neq 1$.

proper mass M_p evaluated on a grid with a grid spacing d , $M_p(d)$, therefore scales according to

$$M_p(d) = M_0 + M_2 d^2 + O(d^3). \quad (4.4)$$

Taking values for different N (and hence d), we can eliminate the second order error term by Richardson extrapolating to $d = 0$, which yields the value M_0 . This is the value that we plotted in Fig. 3. In Table II we summarize these results by tabulating the masses $M_p(d)$ for the different grid resolutions, together with the Richardson extrapolated value M_0 .

Comparing M_0 with $M_p(d)$ for $N = 60$ and 75, we find deviations of $\sim 0.6\%$ and $\sim 0.4\%$, respectively. This is a lower limit on the truncation error that we have to expect in the subsequent evolution.

Note that in Fig. 3, we plot the mass versus maximum density for a sequence of constant separation (namely for contact binaries). In this graph, the onset of instability need not coincide with the maximum mass configuration. Instead, the onset of instability can be located by constructing sequences of constant angular momentum (see Baumgarte *et al.* [17]). However, we expect that the onset of instability is very close to the maximum mass configuration. We therefore present results for two models, one with a maximum density slightly less than the maximum mass model (denoted Ba, $\rho_{max} = 5 \times 10^{-5}$), and one with a maximum density slightly larger (Da,

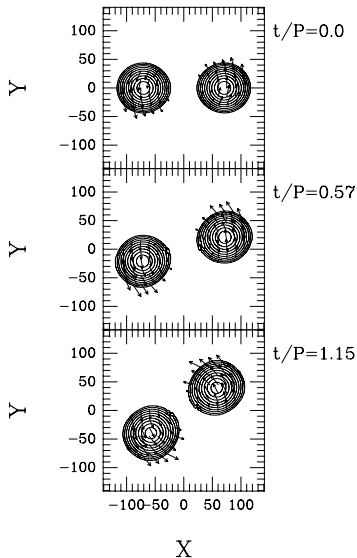


FIG. 5. Snapshots of density contour lines and the velocity flow (v^x, v^y) in the equatorial plane for model Ba. Contour lines are drawn for $\rho_*/\rho_{*0} = 10^{-0.3j}$, where ρ_{*0} denotes the maximum value at $t = 0$, for $j = 0, 1, 2 \dots 10$. Vectors indicate the local velocity field. Time is shown in units of orbital period P . See Table I for the relation between P and $\rho_{\max,0}$.

$\rho_{\max} = 1.5 \times 10^{-4}$). For both models, the orbital period is ~ 50 in units of $\rho_{\max,0}^{-1/2}$ where $\rho_{\max,0}$ is maximum value of ρ at $t = 0$.

In Fig. 4, we show the time evolution of the maximum value of ρ_* ($\rho_{*\max}$) for models Ba and Da. We show results for three different grid resolutions, $N = 50, 60$, and 75 , where we have kept the location L of the outer boundary constant. We picked L such that each star is covered by $\sim N/2 - 5$ grid points (see Table I).

For model Da, we also picked several different values of K , and marked all simulations with $K \neq 1$ accordingly in Fig. 4. Depending on K , these models either collapse or expand, but never oscillate stably. This indicates that they are dynamically unstable, as we have expected. As in the discussion of unstable spherical models, we would expect the cutoff between initial expansion and contraction to be at $K = 1$ if we had arbitrary accuracy. This is not the case, but we again find that increasing the grid resolution makes this cutoff approach unity (cutoff value of K is less than 0.99 for $N = 50$, $\simeq 0.992$ for $N = 60$, and $\simeq 0.995$ for $N = 75$).

For model Ba, we only show results for $K = 1$. Obviously, this configuration oscillates stably. The oscillations are due to a slight inconsistency between the initial data and the evolution scheme. The amplitude of these oscillations decreases with increasing grid number, which shows that our method is convergent. Note that M_0 of this

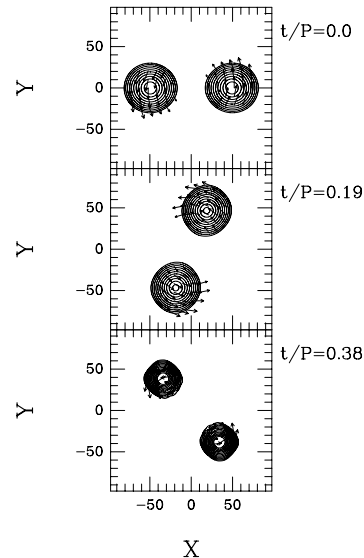


FIG. 6. Same as Fig. 5, except for model Da at $t = 0$. For this sequence we set $K = 0.994$ initially.

configuration is 1.250 , which is marginally larger than the maximum allowed rest mass of an isolated, spherical star, $M_{\max} = 1.248$. We therefore conclude that *all stars that are stable in isolation are also stable in a corotational binary*. We expect that the reverse is not true: a star in a close binary can support more mass than an isolated, spherical star. Note that our results are different from those of WMM, who found that stars with masses of as much as 10 % or more below the maximum allowed rest mass in isolation were destabilized in a close binary. At this level, such an effect would be discerned easily by our code, but it is not present.

In Figs. 5 and 6, we show contour lines of ρ_* and the velocity field of (v^x, v^y) in the equatorial plane for models Ba and Da, using a grid resolution of $N = 75$. For model Da we set $K = 0.994$. Note that for our adopted soft equation of state, the stars are very centrally condensed. The tidal field mostly deforms the very low density envelope, which is hardly visible in these plots. The two envelopes are pulled towards the binary companion, and in our contact cases, touch at the origin. The high density cores, however, are hardly deformed by the tidal field, and are still fairly far separated.

For model Ba, we show contours at $t = 0.0, 27.0$, and 55.5 , all in units of $\rho_{\max,0}^{-1/2}$, which corresponds to the initial condition, a little more than half an orbital period, and a little over an orbital period. It is obvious from the graphs that the two stars stably orbit each other. Note also that the velocity field remains close to being corotational, and that we do not see any evidence of vorticity features which have been reported in ref. [8].

For model Da we show contours at $t = 0.0, 9.55$ and

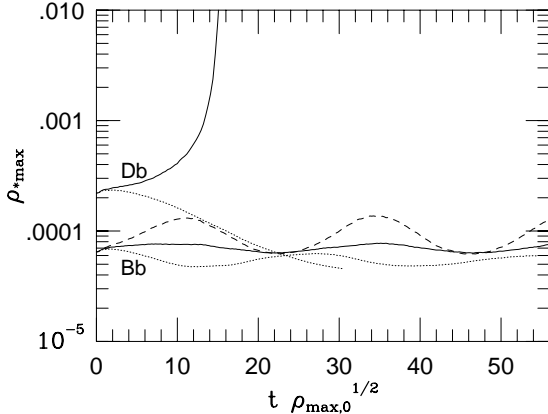


FIG. 7. Time evolution of ρ_{*max} in the corotational, near-equilibrium binary models Bb and Db. Initially, we set $K = 0.98$ (dotted line), $K = 0.975$ (solid line) and $K = 0.97$ (dashed line) for model Bb, and $K = 0.98$ (dotted line) and $K = 0.975$ (solid line) for model Db. For models Bb and Db, the orbital period is ~ 39 and $46\rho_{max,0}^{-1/2}$.

$19.1\rho_{max,0}^{-1/2}$, which is a little less than half an orbital period. It can be seen very clearly how the star contracts and collapses.

B. Corotational near-equilibrium models

We now present numerical results for our corotational near-equilibrium models. We do this to calibrate our code, and to show that our near-equilibrium models are good approximations to self-consistent equilibrium models [32]. This justifies studying such near-equilibrium models for irrotational binaries.

For all the simulations discussed in this and the following subsection, we use a numerical grid with $N = 60$ grid points. We adjust the outer boundary L such that the radius of each star is covered with ~ 25 grid points. For the models Bb and Bc we used $L = 125$ and for Db and Dc $L = 96$ (see Table I). We construct spherical models, and placed them on the grid such that their centers of mass is located at $(x, y, z) = (\pm L/2, 0, 0)$. Note that these stars are not in contact. However, the stars are not tidally deformed, and therefore separation of the center of masses of the two stars is slightly smaller than for the self-consistent equilibrium models. The orbital period for these binaries is ~ 39 and 46 in units of $\rho_{max,0}^{-1/2}$, respectively.

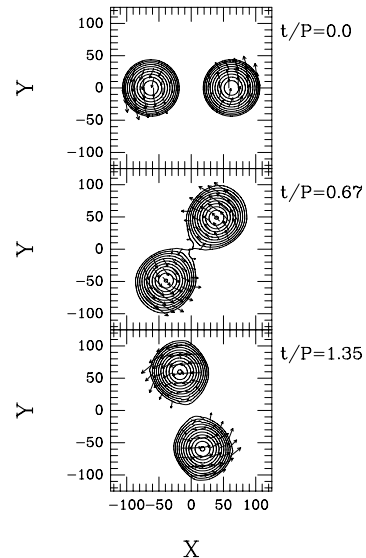


FIG. 8. Same as Fig. 5, but for model Bb. For this sequence we set $K = 0.975$ initially.

In Fig. 7, we show the time evolution of ρ_{*max} for models Bb and Db. Dotted, solid and dashed lines denote results for $K = 0.98$, 0.975 and 0.97 , respectively. As before, model Db either expands or contracts, but never oscillates stably. We again conclude that Db is dynamically unstable. Model Bb, on the other hand, exhibits stable oscillation for several different values of K , and we conclude that it is dynamically stable.

It is interesting to note that even with a reduced value of $K = 0.98$, model Bb initially expands, albeit stably. Only reducing the pressure to a value smaller than that ($K \sim 0.975$), the configuration is roughly in equilibrium. This can be understood quite easily, because the spherical star is not a self-consistent equilibrium solution. The tidal field tends to deform the star, which reduces the central density. Therefore, our initial data have too high a central density for their mass, and the star starts expanding. This can be compensated for by reducing K and hence the pressure. As we have argued before, reducing K is equivalent to increasing the mass, and indeed this is another way of understanding why a star in a binary can support more mass than a star in isolation.

In Fig. 8, we show contour lines of ρ_* and the velocity field (v^x, v^y) in the equatorial plane for model Bb, where we have set $K = 0.975$. We show the configuration at $t = 0.0, 26.5$ and $53.0\rho_{max,0}^{-1/2}$. Comparing these plots with Fig. 5, one can see that the center of masses of the two stars are closer. During the evolution, the stars lose their spherical shape and adjust to the tidal field. However, all the qualitative features are very similar to the self-consistent equilibrium simulations. In particular, the velocity field remains nearly corotational, and we do not

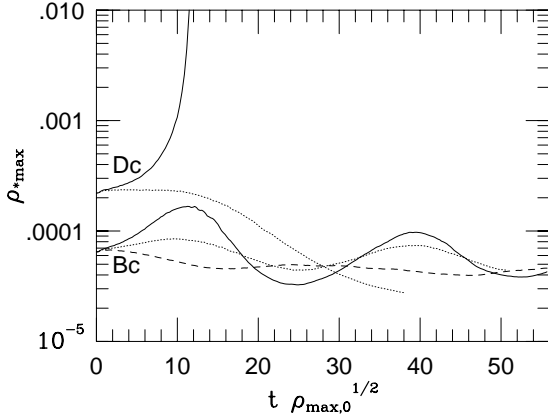


FIG. 9. Time evolution of ρ_{*max} in the irrotational, near-equilibrium binary models Bc and Dc. Initial values of K are 0.99, 0.985 and 0.98 for model Bc, and 0.98 and 0.985 for model Dc. Solid, dotted and dashed lines denote results for $K = 0.98, 0.985$ and 0.99 , respectively. The orbital period of models Bc and Dc is ~ 39 , and $46\rho_{max,0}^{-1/2}$, again.

see any evidence of the double vorticity fields as reported by WMM.

This test suggest that the spherical near-equilibrium models are very good approximations to self-consistent equilibrium configurations for the models and issues we are investigating here (but see footnote [32]).

C. Irrotational near-equilibrium models

Viscosities in neutron stars are expected to be too small to bring neutron star binaries into corotation on the timescale of their evolution [28]. Numerical models exist only in Newtonian gravity [29,30] or in the Newtonian and post-Newtonian ellipsoidal approximation [22,11]. We therefore adopt the spherical near-equilibrium approximation to construct initial models, which we have calibrated and found to be adequate in section IV.B for corotational cases.

We again vary K and choose $K = 0.99, 0.985$ and 0.98 for model Bc, and $K = 0.985$ and 0.98 for model Dc. In Fig. 9, we show time evolution of ρ_{*max} for models Bc and Dc. Dashed, dotted and solid lines denote results for $K = 0.99, 0.985$ and 0.98 , respectively. As in the corotational cases, model Dc cannot be held stably, whereas model Bc oscillates for all these choices of K . Therefore, we again conclude that model Bc is dynamically stable, whereas Dc is not.

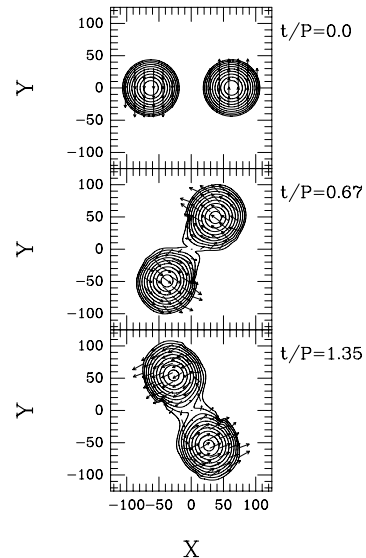


FIG. 10. Same as Fig. 5, but for model Bc. For this sequence, we set $K = 0.99$ initially.

It is interesting to note that for these irrotational models, we had to reduce K by a somewhat smaller amount to minimize the amplitude of oscillations in model Bc than for the corotational model Bb ($K \sim 0.985$ here, and $K \sim 0.975$ for model Bb). This can be understood very easily, because in corotational models, the individual stars are spinning, and are therefore stabilized and deformed by both the tidal field and the their own spin. In irrotational binaries, the stars have almost no spin (with respect to distant inertial observers), and are deformed only by the tidal field. Therefore, putting a star into an irrotational binary will reduce the central density by less than putting the same star into a corotational binary. As a consequence, we have to reduce K by a smaller amount to compensate. Applying our scaling argument, this result means that a irrotational binary can support less mass than a corotational binary, but still more than a spherical star in isolation. This result is corroborated by the post-Newtonian ellipsoidal models constructed in [11].

In Fig. 10, we show contour lines of ρ_* and the velocity field (v^x, v^y) in the equatorial plane for model Bc and $K = 0.99$ initially. We show contours at $t = 0.0, 26.5$, and $53.0\rho_{max,0}^{-1/2}$. For the bulk of the matter at the core of the stars, the velocity field remains approximately irrotational, and the stars stably orbit each other. We conclude that there is no qualitative difference between corotational and irrotational binaries as far as their radial stability properties are concerned.

V. SUMMARY

We perform post-Newtonian, dynamical simulations of close binaries in circular orbit. In particular, we study the stability of the individual stars against gravitational collapse in both corotational and irrotational systems containing stars of equal mass.

We have chosen a soft, adiabatic equation of state with $\Gamma = 1.4$, for which there is no innermost stable circular orbit, so that the binary *orbit* is stable even when the stars are in contact, and for which the onset of instability for a spherical star in isolation occurs at a very small value of the compaction M/R . We can therefore study the individual stars' stability properties in near contact binaries, for which the tidal effects are strongest, and in a regime in which a post-Newtonian approximation is very accurate.

We do not find any crushing effect as reported by WMM [8]. In contrast, the maximum density in both corotational and irrotational binaries is smaller than that of spherical stars in isolation. We find that stars in binaries can support more mass than in isolation. Moreover, all stars that are stable against radial perturbations in isolation, will also be dynamically stable when put into a binary.

All these results are in complete agreement with, for example, the findings of Baumgarte *et al.* [16,17], Flanagan [14], and Thorne [15]. For the most part, their discussions rigorously address *secular* stability only. Several different arguments can be invoked to suggest that *secularly* stable binaries are also *dynamically* stable, but this is strictly proven only in Newtonian theory (see also [11]). Our dynamical calculations reported in this paper are the first to directly confirm dynamical stability, at least within our post-Newtonian approximation.

We compare, in a near-equilibrium approximation, corotational and irrotational binary models. As expected, stars in corotational binaries can support slightly more mass than in irrotational binaries, but apart from these small differences we do not find any qualitative difference in their radial stability properties. A more rigorous treatment will require the construction of post-Newtonian, irrotational equilibrium binary models for initial data.

Since our computations have been performed in nondimensional units, our results apply not only to neutron star binaries, but also to binaries of white dwarfs and supermassive stars. In fact, the equations of state of massive white dwarfs (ideal degenerate, extremely relativistic electrons) and supermassive stars (radiation \gg thermal pressure) are closely approximated by the value $\Gamma = 1.4$ that we have adopted. These binaries may be important low frequency gravitational wave sources for future space-based gravitational wave detectors, like LISA.

ACKNOWLEDGMENTS

Numerical computations were performed on the FACOM VX/4R machine in the data processing center of the National Astronomical Observatory of Japan. M. S. wishes to express his gratitude to the University of Illinois at Urbana-Champaign for its hospitality during his stay in September, 1997, when this project was initiated. This work was supported by a Japanese Grant-in-Aid of the Ministry of Education, Culture, Science and Sports (Nos. 08NP0801 and 09740336), and by NSF Grant AST 96-18524 and NASA Grant NAG 5-3420 at Illinois.

-
- [1] S. E. Thorsett, Z. Arzoumanian, M. M. McKinnon and J. H. Taylor, *Astrophys. J.* **405**, L29 (1993).
 - [2] J. H. Taylor and J. M. Weisberg, *Astrophys. J.* **345**, 434 (1989).
 - [3] A. Abramovici, et al. *Science* **256**, 325 (1992).
 - [4] C. Bradaschia, et al. *Nucl. Instrum. and Methods* **A289**, 518 (1990).
 - [5] K. Kuroda et al. in *Proceedings of the international conference on gravitational waves: Sources and Detectors*, edited by I. Ciufolini and F. Fiducard (World Scientific, 1997), p.100.
 - [6] J. Hough, in *Proceedings of the Sixth Marcel Grossmann Meeting*, edited by H. Sato and T. Nakamura (World Scientific, Singapore, 1992), p.192.
 - [7] T. W. Baumgarte, S. L. Shapiro, G. B. Cook, M. A. Scheel, and S. A. Teukolsky, *Phys. Rev. D*, in press, gr-qc/9709026.
 - [8] J. R. Wilson and G. J. Mathews, *Phys. Rev. Lett.* **75**, 4161 (1995); J. R. Wilson, G. J. Mathews and P. Maronetti, *Phys. Rev. D* **54**, 1317 (1996); gr-qc/9710140 (WMM)
 - [9] D. Lai, F. A. Rasio and S. L. Shapiro, *Astrophys. J. Suppl.* **88**, 205 (1993).
 - [10] D. Lai, *Phys. Rev. Lett.* **76**, 4878 (1996).
 - [11] J. C. Lombardi, F. A. Rasio and S. L. Shapiro, 1997, *Phys. Rev. D*, in press (astro-ph/9705218).
 - [12] A. G. Wiseman, *Phys. Rev. Lett.* **79**, 1189 (1997).
 - [13] P. R. Brady and S. A. Hughes, *Phys. Rev. Lett.* **79**, 1186 (1997).
 - [14] E. E. Flanagan, gr-qc/9706045.
 - [15] K. S. Thorne, gr-qc/9706057.
 - [16] T. W. Baumgarte, S. L. Shapiro, G. B. Cook, M. A. Scheel, and S. A. Teukolsky, *Phys. Rev. Lett.* **79**, 1182 (1997).
 - [17] T. W. Baumgarte, S. L. Shapiro, G. B. Cook, M. A. Scheel, and S. A. Teukolsky, *Phys. Rev. D* **57**, 6181 (1998).
 - [18] S. Chandrasekhar, *Astrophys. J.* **140**, 417 (1964); **142**, 1519 (1965).
 - [19] S. Chandrasekhar, *Astrophys. J.* **142**, 1488 (1965).
 - [20] R. Reith and G. Schäfer, gr-qc/9603043.

- [21] H. Asada, M. Shibata, and T. Futamase, *Prog. Theor. Phys.* **96**, 81 (1996);
H. Asada and M. Shibata, *Phys. Rev. D* **54**, 4944 (1996).
- [22] D. Lai, F. A. Rasio and S. L. Shapiro, *Astrophys. J.* **420**, 811 (1994)
- [23] Newtonian and post-Newtonian considerations illustrate the physical meaning of ${}_{(n)}\alpha$, ${}_{(n)}\psi$, ${}_{(n)}\beta^i$, and ${}_{(n)}h_{ij}$ for $n \neq 0$. The terms ${}_{(2)}\alpha$, ${}_{(2)}\psi$, ${}_{(1)}\beta^i$, and ${}_{(2)}h_{ij}$ do not affect the dynamics of the stars; effects due to tidal deformation of spherical stars appear at $n = 6$ in ${}_{(n)}\alpha$ and ${}_{(n)}\psi$, at $n = 7$ in ${}_{(n)}\beta^i$, and at $n = 8$ in ${}_{(n)}h_{ij}$; effects of gravitational radiation are included in ${}_{(n)}h_{ij}$ for $n \geq 5$, in ${}_{(n)}\alpha$ and ${}_{(n)}\psi$ for $n \geq 7$, and in ${}_{(n)}\beta^i$ for $n \geq 8$ [21]. We also note that in Eqs. (2.30)–(2.33), gauge dependent terms (e.g., terms such as ${}_{(5)}h_{ij}$ that may be erased by a gauge transformation) are included, because they appear in our gauge condition.
- [24] M. Shibata, K. Oohara and T. Nakamura, *Prog. Theor. Phys.* **98**, 1081 (1997).
- [25] S. L. Shapiro and S. A. Teukolsky, *Black Holes, White Dwarfs, and Neutron Stars* (Wiley, New York, 1983), chapter 6.
- [26] Note that for the case where the star expands, we stopped the computation when the surface of the star reached the outer boundary of numerical grid. Since the star is gravitationally bound, the star ultimately has to recontract and collapse.
- [27] M. Shibata, *Phys. Rev. D* **55**, 6019 (1997); *Prog. Theor. Phys.* **96**, 317 (1996).
- [28] C. S. Kochanek, *Astrophys. J.* **398**, 234 (1992);
L. Bildsten and C. Cutler, *Astrophys. J.* **400**, 175 (1992)
- [29] K. Uryu and Y. Eriguchi, astro-ph/9712203.
- [30] S. Bonazzola, E. Gourgoulhon and J.-A. Marck, *Phys. Rev. D* **56**, 7740 (1997); see also talk at GRG 15, India (1997).
- [31] Strictly speaking, the irrotational condition for the perfect fluid in the (3+1) formalism is $\tilde{u}_{i,j} - \tilde{u}_{j,i} = 0$ (M. Shibata, preprint OU-TAP 73, unpublished). Here, however, $\Gamma\epsilon \ll 1$, so that Eq. (4.2) may be regarded as an approximate irrotational condition (cf. Eq.(2.9)).
- [32] For stiffer equations of state with higher Γ , the bulk of the mass would suffer greater tidal distortion at the same separation. Our near-equilibrium spherical approximation would require larger orbital separations, and hence more numerical resolution, to be as reliable in these cases.

Table I. Initial conditions of binary models. We tabulate the maximum density $\rho_{\max,0}/10^{-5}$, the radius R_∞ of a spherical star of the same rest mass in isolation, the orbital period P in units of $\rho_{\max,0}^{-1/2}$, the nature of the initial velocity field and matter profile, and the location of the outer boundary L (see text). All quantities are shown in units of $c = G = K = 1$.

Model	$\rho_{\max,0}/10^{-5}$	R_∞	$P \times \sqrt{\rho_{\max,0}}$	Velocity Field	Matter Profile	L
Ba	5	53	48.6	corotation	equilibrium	141
Da	15	38	50.2	corotation	equilibrium	97.5
Bb	5	53	39.4	corotation	spherical	125
Db	15	38	45.9	corotation	spherical	96
Bc	5	53	39.4	irrotation	spherical	125
Dc	15	38	45.9	irrotation	spherical	96

Table II. Proper mass M_p of each star in a corotational equilibrium binary for different grid resolutions. We tabulate M_p versus central density ρ_c for $N = 40, 50, 60,$ and 75 . We also list the Richardson extrapolated value M_0 as well as the proper mass of the spherical model in isolation with the same central density.

$\rho_c/10^{-5}$	2	5	10	15
$N = 40$	1.1954	1.2347	1.2469	1.2451
$N = 50$	1.2004	1.2402	1.2526	1.2509
$N = 60$	1.2031	1.2431	1.2556	1.2539
$N = 75$	1.2051	1.2455	1.2581	1.2565
M_0	1.209	1.250	1.263	1.261
Spherical	1.1933	1.2344	1.2482	1.2476